PAPER

Modified embedded-atom method interatomic potential for Mg–Y alloys

IOP Publishing Modelling and Simulation in Materials Science and Engineering

Modelling Simul. Mater. Sci. Eng. **26** (2018) 065010 (25pp) https://doi.org/10.1088/1361-651X/aacfd2

Modified embedded-atom method interatomic potential for Mg–Y alloys

Rasool Ahmad[1], Sébastien Groh[2], Maryam Ghazisaeidi[3] and William A Curtin[1]

[1] Laboratory for Multiscale Mechanics Modeling, Institute of Mechanical Engineering, EPFL, 1015 Lausanne, Switzerland
[2] Department of Biomedical Engineering, University of Basel, 4123 Allschwil, Switzerland
[3] Department of Materials Science and Engineering, The Ohio State University, Columbus, OH 43210, United States of America

E-mail: rasool.ahmad@epfl.ch

Received 4 May 2018, revised 22 June 2018
Accepted for publication 28 June 2018
Published 20 July 2018

Abstract

An interatomic potential for the Mg–Y binary system is developed within the framework of the second-nearest-neighbor modified embedded-atom method (MEAM) based on a very good MEAM potential for pure Mg. The Mg–Y potential is fitted to a range of key physical properties, either experimental or computed by first-principles methods, including the Y interaction energy with basal and pyramidal stacking faults, and properties of the B2 Mg–Y intermetallic phase. Reasonable agreement is obtained—much better than existing potentials in the literature—but differences remain for subtle but important aspects of Y solutes in Mg. The predictions of the potential for Y misfit volume in Mg, Y solute interactions with the pyramidal II $\langle \boldsymbol{c}+\boldsymbol{a}\rangle$ edge dislocation and $\{10\bar{1}2\}\langle\bar{1}011\rangle$ tension-twin boundary are then compared against recent density functional theory results, and reasonable accuracy is obtained. In light of the spectrum of results presented here, the applicability and limitations of this Mg–Y MEAM potential for investigating various plasticity phenomena in Mg–Y solid solution alloys are carefully discussed.

Supplementary material for this article is available online

Keywords: MEAM, interatomic potential, Mg–Y alloy, molecular dynamics

(Some figures may appear in colour only in the online journal)

1. Introduction

Magnesium (Mg) is the lightest structural metal, having a density two thirds that of Al and one quarter that of Fe, and has a high potential for applications in the automotive, aerospace and biomedical industries [1–3], the latter due to the good biocompatability of Mg. However, wide use of Mg is significantly inhibited by its low ductility and low fracture toughness at room temperature. The hexagonally closed-packed (hcp) crystal structure leads to high anisotropy in the stresses needed to move dislocations on different slip systems, e.g. the critical resolved shear stress for pyramidal $\langle \boldsymbol{c} + \boldsymbol{a} \rangle$ slip is almost two orders of magnitude higher than that for $\langle \boldsymbol{a} \rangle$ slip on basal plane [4, 5]. This slip anisotropy is largely due to an intrinsic thermally activated transformation of $\langle \boldsymbol{c} + \boldsymbol{a} \rangle$ dislocations from easy-glide pyramidal planes to basal plane [6–8] having a low-energy barrier (0.3 eV for pyramidal I mixed [9] and 0.5 eV for pyramidal II edge dislocation [10]). These features of the $\langle \boldsymbol{c} + \boldsymbol{a} \rangle$ dislocations render Mg unable to easily accommodate the $\langle \boldsymbol{c} \rangle$ axis deformation necessary to satisfy the von Mises criterion for general plasticity [11].

Experiments show that solid solution alloying of Mg with yttrium (Y) and other rare earth elements significantly enhances the room temperature ductility of the resulting Mg alloys [12–14]. Enhanced ductility is accompanied by an increased activity of $\langle \boldsymbol{c} + \boldsymbol{a} \rangle$ slip systems [15, 16]. The ductility is in part connected to weaker basal textures, but the mechanisms leading to weaker texture and enhanced $\langle \boldsymbol{c} + \boldsymbol{a} \rangle$ activity have not yet been definitively identified. One recent possible explanation involves the basal I_1 stacking fault, and its energy variations with solute type [17, 18]. However, recent density functional theory (DFT) calculations [19] suggest no correlation between I_1 stacking fault energy and observed ductility across various solutes. The possibility of Y solute atoms stabilizing the pyramidal $\langle \boldsymbol{c} + \boldsymbol{a} \rangle$ edge dislocations has also been exhausted with no encouraging result [19, 20]. A new mechanism explaining the origin of ductility in Mg alloys has been recently discovered by Wu *et al* [16] which is based on the role of solutes in accelerating $\langle \boldsymbol{c} + \boldsymbol{a} \rangle$ cross-slip. The solutes are postulated to reduce the barrier for cross-slip from the low-energy pyramidal II $\langle \boldsymbol{c} + \boldsymbol{a} \rangle$ screw dislocation cross-slipping onto the higher energy pyramidal I planes. This process, and the cross-slip back to the pyramidal II planes, is postulated to generate new mobile dislocation content at a faster rate than the immobilizing pyramidal-to basal transformation, enabling $\langle \boldsymbol{c} + \boldsymbol{a} \rangle$ plasticity at the intrinsic stresses of easy-glide pyramidal slip. This model explains how Y and other rare earth solutes can positively affect ductility and weak texture formation at very low ($<$1 at%) concentrations. First-principles DFT studies provide one avenue for accurate assessment of individual solute interaction energies with dislocation and stacking fault. However, the collective behavior of solutes at finite solute concentrations, and the study of complex dislocation processes and their energy barriers, is not yet computationally feasible via DFT. A deeper understanding of proposed mechanisms can be achieved, in part, through direct atomistic simulations of the mechanisms on realistic representations of the alloys. Such simulations require, then, interatomic potentials for the alloys that capture all the relevant energetics of the various processes. Since Y is perhaps the most widely studied rare earth element found to lead to a ductile Mg alloy at low solute concentrations, the development of accurate interatomic potentials for the binary Mg–Y system is particularly valuable; this is thus the goal of the present paper.

Because of its importance, previous researchers have created Mg–Y potentials. Kim *et al* [21] developed an Mg–Y alloy potential using the framework of the second-nearest-neighbor modified embedded-atom method (MEAM). This potential, hereafter, referred to as the Kim potential, describes the structural and elastic properties of stable Mg–Y intermetallic compounds in reasonable agreement with experimental and first principal data. However, the

predicted Y misfit volume is much smaller than experiments and DFT. The Kim potential also predicts very weak effect of Y on the basal (I_1 and I_2) and pyramidal I (SF2) stable stacking fault energies. Pei *et al* [22] proposed an EAM potential for Mg–Y alloys and conducted a detailed study on the generalized stacking fault energy in different slip system for pure Mg and Mg–Y alloy, but this potential has not been tested for the dislocation properties in pure Mg. Since achieving stacking fault energies in agreement with DFT does not ensure good predictions of dislocation properties [5, 23], this EAM potential warrants further validation before its application in plasticity and dislocation related problems.

Here, we present a new MEAM interatomic potential for the Mg–Y binary system that is fitted to a range of properties relevant to plasticity. The potential is based on the recent MEAM potential for pure Mg [5], which yields excellent agreement with a wide range of experimental and/or DFT-computed properties of pure Mg. The fitting leads to generally good agreement for the Y misfit volume, interaction energies of Y atom with various stacking faults (basal I_1, basal I_2, basal E, pyramidal I SF2, pyramidal I SF3 and pyramidal II SF) and heat of formation of the Mg–Y B2 intermetallic. The potential is then compared with DFT for Y interactions with the pyramidal II $\langle \boldsymbol{c}+\boldsymbol{a}\rangle$ edge dislocation and with $\{10\bar{1}2\}\langle\bar{1}011\rangle$ tension-twin boundary and for other intermetallic compounds, and reasonable agreement is found. However, the potential is not perfect and deviates sufficiently for various subtle properties so as to make it unsuitable for all possible applications, in particular for assessing pyramidal II-I cross-slip. We thus discuss the problems for which this Mg–Y potential, which may exhaust the capability of the second-nearest-neighbor MEAM framework, can be utilized productively to test specific mechanisms and enable quantitative comparisons between theory and simulations on the approximate Mg–Y system.

The remainder of this paper is arranged as follows. In section 2, we provide a brief description of the MEAM potential and the optimized potential parameters for Mg–Y binary alloys as determined here. In section 3, the heats of formation, lattice constants, and elastic constants for different Mg–Y intermetallic compounds are presented. In section 4, the Y misfit volume in Mg, Y solute–solute interaction energy and interaction energies of Y with various stacking faults are shown, some of which were used in the fitting. Sections 5 and 6 present the interaction energy of Y with the pyramidal II $\langle \boldsymbol{c}+\boldsymbol{a}\rangle$ edge dislocation and $\{10\bar{1}2\}\langle\bar{1}011\rangle$ tension-twin boundary, respectively, which were not involved in the fitting procedure. In section 7, we discuss the scope of applications where this Mg–Y MEAM potential can be useful. All computations using the MEAM potential are performed using the LAMMPS package [24] and visualizations created using the OVITO code [25].

2. MEAM potential for Mg–Y binary alloy

The MEAM interatomic potential framework was first proposed by Baskes [26, 27] as a modification of the EAM potential method to account for the directionality of near-neighbor atomic bonding. The MEAM was later modified to overcome some critical shortcomings of the original formalism [28, 29], primarily by including second-nearest-neighbor interactions. The framework for the MEAM interatomic potential is described in the appendix. To describe a binary alloy within the MEAM formalism first requires interatomic potentials of the constituent elements. For pure Mg, we use the MEAM potential of Wu *et al* [5], which accurately describes many properties pertaining to plastic deformation and fracture such as various stacking fault energies, dislocation core structures, and Peierls stresses. An MEAM potential for pure Y was developed by Ko and Lee [30], which is also used in Kim potential, and describes structural and mechanical properties in good agreement with experimental data.

Table 1. MEAM potential parameters used here for pure Mg and Y. The units of E_c, r_e and B are eV, Å and 10^{12} dyne cm^{-2}, respectively.

	E_c	r_e	B	A	$\beta^{(0)}$	$\beta^{(1)}$	$\beta^{(2)}$	$\beta^{(3)}$	$t^{(1)}$	$t^{(2)}$	$t^{(3)}$	$C_{\min}$	$C_{\max}$	d
Mg	1.51	3.18	0.37	0.52	2.00	1.30	1.30	1.00	5.55	3.00	−7.40	0.49	2.80	0.00
Y	4.37	3.607	0.448 6	0.90	2.00	5.00	1.00	1.00	8.00	8.00	−8.50	0.36	2.80	0.00

Table 2. Cohesive energy (E_c), lattice constants (a and c/a), elastic constants (C_{11}, C_{12}, C_{13}, C_{33}, C_{44}), structural energy difference ($\Delta E_{\text{hcp}\rightarrow\text{fcc}}$ and $\Delta E_{\text{hcp}\rightarrow\text{bcc}}$), basal surface energy, and relaxed vacancy formation energy (E_v^f) of Y element as calculated from the current MEAM potential and the Kim potential, along with existing experimental and DFT values. Units of each property are mentioned in the parentheses in the second column.

Properties		MEAM	Kim potential	DFT/ experimental
Cohesive energy	E_c (eV/atom)	−4.373	−4.374[a]	−4.28[a], −4.37[b]
Lattice constants	a(Å)	3.641	3.645[a]	3.659[a], 3.647[c]
	c/a	1.598	1.580[a]	1.549[a], 1.571[c]
Elastic constants	C_{11} (GPa)	80.28	77.74[a]	80.40[a], 83.40[d]
	C_{12} (GPa)	20.91	30.00[a]	17.06[a], 29.10[d]
	C_{13} (GPa)	26.18	28.21[a]	15.85[a], 19.00[d]
	C_{33} (GPa)	79.41	75.32[a]	82.88[a], 80.10[d]
	C_{44} (GPa)	29.46	21.71[a]	26.81[a], 26.90[d]
Structural energy difference	$\Delta E_{\text{hcp}\rightarrow\text{fcc}}$ (eV/atom)	0.0334	0.0385[a]	0.0260[a]
	$\Delta E_{\text{hcp}\rightarrow\text{bcc}}$ (eV/atom)	0.1328	0.129[a]	0.125[a]
Surface energy	basal (0001) (mJ m^{-2})	1269	1660[a]	1506[e]
Relaxed vacancy formation energy	E_v^f (eV/atom)	1.391	1.890[a]	1.840[a]

[a] Ko and Lee [30].
[b] Kittel [32].
[c] Spedding *et al* [33].
[d] Simmons and Wang [34].
[e] Vitos *et al* [35].

A full description of a pure element in the MEAM framework requires 14 parameters. Four parameters (cohesive energy E_c, equilibrium nearest-neighbor distance r_e, bulk modulus B, and an adjustable parameter d to fit $\partial B/\partial P$) are obtained from the universal equation of state [31]. Seven parameters (decay lengths ($\beta^{(0)}$, $\beta^{(1)}$, $\beta^{(2)}$, $\beta^{(3)}$) and weight factors ($t^{(1)}$, $t^{(2)}$, $t^{(3)}$)) describe the electron density for embedding. One parameter A is used in the embedding function, and two parameters (C_{min}, C_{max}) account for many-body screening effects. We retain all the literature values for these properties for both Mg and Y, with the exception of the decay parameters $\beta^{(1)}$ and $\beta^{(3)}$ for Y, which are adjusted to better describe the interaction energies of Y solutes with the various stacking faults of Mg. The fourteen parameters for both Mg and Y are shown, following the notation of Kim *et al* [21], in table 1. Various properties of pure Y as predicted by the MEAM potential are presented in table 2, and compared with Kim potential and available DFT and experimental results.

To describe a binary alloy, 13 additional parameters are needed. Four parameters (E_c, r_e, B, d) are related to the universal equation of state for a reference intermetallic compound. Eight parameters related to screening (C) and one parameter related to the electron density scaling (ρ_0^{Mg}:ρ_0^{Y}) are introduced. Potential parameters are fitted using structural and elastic properties of reference B2-MgY structure, the heat of formation of B2-MgY, and the position-dependent single-solute interaction energies with the stable stacking faults on the basal (I_2), pyramidal II and pyramidal I (SF2) planes. Following the notations of Kim *et al* [21], the

Table 3. MEAM potential parameters developed here for binary Mg–Y alloy system. The units of E_c, r_e and B are eV, Å and 10^{12} dyne cm^{-2}, respectively.

Parameters	Values	Parameters	Values
Reference	B2-type Mg–Y	$C_{\min}$(Mg, Y, Mg)	0.60
E_c	3.075	$C_{\min}$(Y, Mg, Y)	0.36
r_e	3.257 5	$C_{\min}$(Mg, Mg, Y)	0.00
B	0.409	$C_{\min}$(Mg, Y, Y)	1.20
d	0.00	$C_{\max}$(Mg, Y, Mg)	2.80
ρ_0^{Mg}:ρ_0^{Y}	1:1.4	$C_{\max}$(Y, Mg, Y)	2.80
		$C_{\max}$(Mg, Mg, Y)	1.63
		$C_{\max}$(Mg, Y, Y)	2.80

fitted parameters for the binary Mg–Y system are shown in table 3. We use radial cutoff distance r_c of 5.875 Å and smoothing radius Δr of 1.875 Å. The potential files of the MEAM potential proposed here are provided in LAMMPS format as the supplementary data, available online at stacks.iop.org/MSMS/26/065010/mmedia. In the following sections we show the specific values obtained in the fitting as compared to the target quantities and then analyze further properties against available experimental and DFT data.

3. Mg–Y intermetallic compounds

The heat of formation for the compound $\mathrm{Mg}_n\mathrm{Y}_m$ is calculated as

$$\Delta H = E_{\mathrm{tot}}^{\mathrm{Mg}_n\mathrm{Y}_m} - \frac{nE_{\mathrm{solid}}^{\mathrm{Mg}} + mE_{\mathrm{solid}}^{\mathrm{Y}}}{n+m}, \tag{1}$$

where $E_{\mathrm{tot}}^{\mathrm{Mg}_n\mathrm{Y}_m}$ represents the total energy of the unit cell of the $\mathrm{Mg}_n\mathrm{Y}_m$ compound, and $E_{\mathrm{solid}}^{\mathrm{Mg}}$ and $E_{\mathrm{solid}}^{\mathrm{Y}}$ represent the energy per atom of Mg and Y in the pure elements.

While the heat of formation for B2-MgY is used to fit the potential, the heats of formation for the C14-$\mathrm{Mg_2Y}$ and A12-$\mathrm{Mg_{24}Y_5}$ intermetallics are calculated to test the domain of validity of the proposed MEAM potential. On one hand, Smith *et al* [36] performed experimental work to quantify the heats of formation of B2-MgY, C14-$\mathrm{Mg_2Y}$ and A12-$\mathrm{Mg_{24}Y_5}$ intermetallics. These authors reported the C14-$\mathrm{Mg_2Y}$ compound to be most stable. On the other hand, Zhang *et al* [37] predicted the heats of formation of the same compounds using first-principles calculations. Unlike Smith *et al* [36], Zhang *et al* [37] reported the B2-MgY compound to be most stable. Among B2-MgY, C14-$\mathrm{Mg_2Y}$ and A12-$\mathrm{Mg_{24}Y_5}$, the A12-$\mathrm{Mg_{24}Y_5}$ compound was the least stable in both experiments and first-principle predictions. Existing semi-empirical Mg–Y potentials predict either C14-$\mathrm{Mg_2Y}$ [22] or B2-MgY [21] to be the most stable. The heats of formation predicted with the current Mg–Y potential are reported in table 4. The convex hull for the current MEAM potential predicts the C14-$\mathrm{Mg_2Y}$ compound to be on the convex hull while the A12-$\mathrm{Mg_{24}Y_5}$ and B2-$\mathrm{Mg_2Y}$ phases are above the convex hull and thus metastable. Finally, the dilute heat of solution of Y alloying element in hcp Mg is predicted to be −0.1 eV, which is overestimated by 50% relative to data reported by Kim *et al* [21]. Therefore, thermodynamics studies with the current potential should be pursued with caution.

The elastic constants of B2-MgY, C14-$\mathrm{Mg_2Y}$, and A12-$\mathrm{Mg_{24}Y_5}$ are calculated using the method proposed by Beckstein *et al* [44], with all atomic positions fully relaxed after imposing the desired strain. Table 5 shows the lattice constants and elastic constants of the

Table 4. Heat of formation (kJ mol^{-1}) of different Mg–Y compounds as calculated by the current MEAM potential and the Kim potential, along with existing experimental and DFT values.

Structure	MEAM	Kim potential	DFT	Experiment
$Mg_{24}Y_5$ (A12)	−8.40	−5.57[a]	−5.84[b], −5.76[c]	−7.53[d]
Mg_2Y (C14)	−19.60	−10.48[a]	−9.17[b], −11.99[e]	−14.22[d]
MgY (B2)*	−12.88	−12.52[a]	−10.64[b], −10.27[f]	−12.55[d]

Note: the asterisk(∗) denotes the properties used in the parameterization of the MEAM potential.
[a] Kim *et al* [21].
[b] Zhang *et al* [37].
[c] Zheng *et al* [38].
[d] Smith *et al* [36].
[e] Chen and Zhang [39].
[f] Chen *et al* [40].

Table 5. Lattice constants (Å) and elastic constants (GPa) of different Mg–Y compounds as calculated from the current MEAM potential and the Kim potential, with existing experimental and DFT values also shown.

Structure	Properties		MEAM	Kim potential	DFT/experimental
$Mg_{24}Y_5$ (A12)	Lattice constant	a	11.24	11.20[a]	11.25[b],11.26[c],11.26[d],11.27[e]
	Elastic constants	C_{11}	75.4	70.0[a]	73.9[d],73.5[e]
		C_{12}	21.7	25.0[a]	22.1[d],19.8[e]
		C_{44}	17.2	14.6[a]	18.0[d],14.8[e]
Mg_2Y (C14)	Lattice constant	a	6.01	6.14[a]	6.04[b],6.05[c],6.06[f],6.05[g]
		c	9.75	9.78[a]	9.75[b], 9.83[g], 9.79[f], 9.81[g]
	Elastic constants	C_{11}	80.4		76.8[f], 73.3[g]
		C_{12}	26.2		25.4[f], 30.5[g]
		C_{13}	23.8		21.1[f], 25.5[g]
		C_{33}	85.5		84.0[f], 78.8[g]
		C_{44}	23.8		17.8[f], 17.6[g]
MgY (B2)*	Lattice constant	a	3.76		3.78[b], 3.80[c], 3.80[d], 3.80[h]
	Elastic constants	C_{11}	59.3	64.6[a]	51.8[d], 52.4[h]
		C_{12}	31.7	35.0[a]	35.8[d], 34.8[h]
		C_{44}	34.9	29.1[a]	37.3[d], 38.73[h]

Note: the asterisk(∗) denotes the properties used in the parameterization of the MEAM potential.
[a] Kim *et al* [21].
[b] Smith *et al* [36].
[c] Zhang *et al* [37].
[d] Ganeshan *et al* [41].
[e] Wang *et al* [42].
[f] Chen and Zhang [39].
[g] Zeng *et al* [43].
[h] Chen *et al* [40].

A12, C14 and B2 intermetallics as obtained from the current MEAM potential along with the Kim potential and DFT/experimental values. For the B2-MgY compound, the potential captures the DFT-computed ranking of elastic constants ($C_{11} > C_{44} > C_{12}$) while the

Kim potential [21] does not. Quantitatively, the current potential predicts elastic constants for the three compounds within 15% of the first-principles data.

4. Y solute properties

4.1. Misfit strain and misfit volume

The first important property of a solute related to mechanical properties of alloys is the solute misfit strain tensor and the associated solute misfit volume. Following [45–47], misfit strains are calculated using the dipole tensor. In simulations, one Mg atom in the perfect hcp lattice is replaced by one Y atom and all atomic positions are then relaxed keeping the periodic cell vectors fixed using periodic boundary conditions. The relaxation leads to the development of stress σ_{ij} in the simulation box containing a solute. The dipole tensor P_{ij} of the solute is related to stress σ_{ij} and total volume of the simulation box V as

$$P_{ij} = -V\sigma_{ij}. \tag{2}$$

The misfit strain of the solute $\varepsilon_{ij}^{\text{misfit}}$ is then computed from dipole tensor P_{ij} using anisotropic elasticity as

$$\varepsilon_{ij}^{\text{misfit}} = \frac{1}{V_0} S_{ijkl} P_{kl}, \tag{3}$$

where S_{ijkl} is the anisotropic compliance tensor of Mg, and V_0 is the volume of one Mg atom in its hcp bulk. The misfit strains are calculated in the coordinate system where $\boldsymbol{x}_1$ is along $[2\bar{1}\bar{1}0]$, $\boldsymbol{x}_2$ along $[01\bar{1}0]$, and $\boldsymbol{x}_3$ is along [0001] direction. The misfit volume of the solute, normalized by the atomic volume of Mg, $\Delta V/V_0$ is the trace of the misfit strain tensor, i.e. $\Delta V/V_0 = \text{tr}(\varepsilon^{\text{misfit}})$.

For the current MEAM potential, we obtain the non-zero misfit strain components $\varepsilon_{11}^{\text{misfit}} = \varepsilon_{22}^{\text{misfit}} = 0.205$ and $\varepsilon_{33}^{\text{misfit}} = 0.183$ for Y in Mg. Wu *et al* [16] report the misfit strain of Y in Mg, using DFT in the same coordinate system, as $\varepsilon_{11}^{\text{misfit}} = \varepsilon_{22}^{\text{misfit}} = 0.223$ and $\varepsilon_{33}^{\text{misfit}} = 0.120$. The DFT misfit strain tensor is thus slightly more anisotropic than that of the MEAM. Previous works on Y usually report only the misfit volume. For the current MEAM potential, the misfit volume is $\Delta V/\ V_0 = 0.593$, in good agreement with DFT values of 0.567 [19], 0.580 [14], and 0.636 [48]. In contrast, the Kim potential yields a value of only 0.240, less than one-half the DFT value. Since the misfit volume is related to the interaction energy of a dislocation with the solute, it is necessary that the potential predicts this quantity accurately for application to many problems in plasticity.

4.2. Solute–solute interaction energy

In the regime of relatively high concentration, the interaction between solute pairs becomes important. Even in dilute alloys, the properties of occasional solute pairs may play some role. In addition, solute–solute interactions drive short-range-order (SRO) by solute–solute repulsion, attraction, or both. The existence of SRO can then affect strengthening of dislocation slip.

Here, we compute the solute–solute interaction energy of Y in Mg for Y solutes on neighboring basal planes. We use a cuboidal simulation box of size $10[2\bar{1}\bar{1}0] \times 10[01\bar{1}0] \times 5[0001]$, periodic in all direction. After substituting two Mg atoms with Y atoms, atomic positions are relaxed keeping the repeat vector of simulation box fixed (relaxation of stresses causes no appreciable difference). To compute the interaction energy, we use the

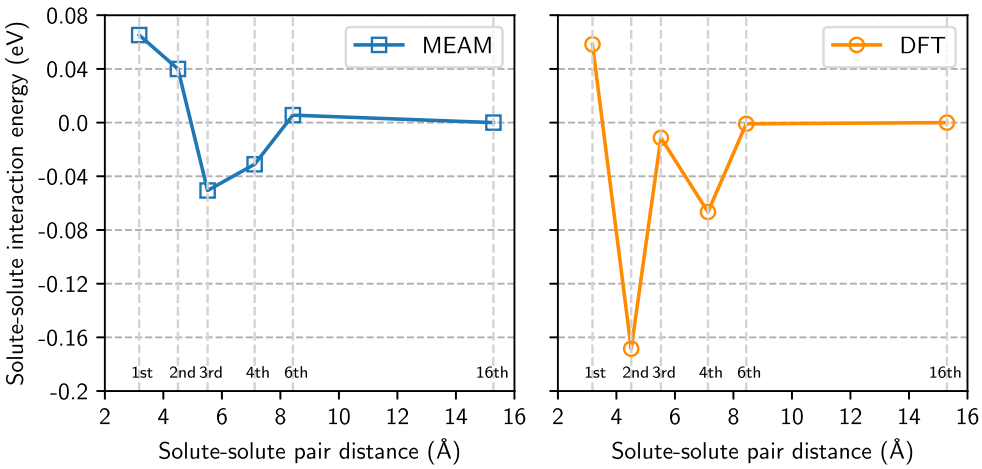

Figure 1. Variation of solute–solute interaction energy of Y in Mg with pair distance, as calculated using (a) MEAM potential and (b) DFT. One solute of each pair is located in one basal plane and other in the neighboring basal plane. Labels on the vertical dotted line denote the order of the neighbor.

energy of the structure having two solutes at 16th neighbor distance as a reference energy. The solute–solute interaction energy is then the energy of the structure containing the solute-pair minus the energy of the reference structure. Figure 1 shows the results of the solute–solute interaction energy obtained from the MEAM potential and DFT (for DFT details, see [16, 19]). Both DFT and the MEAM potential predict the first neighbor Y solutes to be repulsive with nearly same energy. However, DFT predicts the second neighbor solutes to be strongly attractive (energy lower by ≈ -0.168 eV) while the MEAM potential predicts second neighbor solutes to be moderately repulsive. The MEAM also predicts the third neighbor pairs to be moderately attractive (≈ -0.051 eV) while DFT predicts a smaller value (≈ -0.011 eV). Fourth neighbors are predicted to be attractive, but the DFT value is nearly twice that of the MEAM (≈ -0.067 eV versus ≈ -0.031 eV). Thus, solute–solute interactions are not predicted sufficiently well to accurately capture any SRO effects that might arise in Mg–Y. The potential should thus be used for the study of dilute alloys.

Since the DFT interaction is strong, dilute Mg–Y alloys annealed at moderate temperatures could develop the short-range order and exhibit consequent strengthening of basal slip. The slip of a dislocation in the presence of SRO involves the breaking of bonds between energetically favorable solute pairs and the formation of bonds between energetically unfavorable solute pairs across the glide plane. This can lead to a strengthening effect. We will examine this issue in the future.

4.3. Y interaction with stacking faults

4.3.1. Simulation method. To compute solute/stacking fault interaction energies, we adopt the simulation box geometry and methodology used in recent DFT studies of the same problem by Yin *et al* [19]. For each slip system, a primitive cell is defined by a set of three vectors ($\boldsymbol{a}_1$, $\boldsymbol{a}_2$, $\boldsymbol{a}_3$) as shown in figure 2 with ($\boldsymbol{a}_1$, $\boldsymbol{a}_2$) defining the stacking fault plane and $\boldsymbol{a}_1$, $\boldsymbol{a}_2$ and $\boldsymbol{a}_3$ usually not mutually orthogonal. A periodic simulation cell of pure Mg is built by replicating the primitive cell N_i times in the $\boldsymbol{a}_i (i = 1, 2, 3)$ directions to obtain a parallelopiped simulation cell with periodic repeat vectors ($N_1\boldsymbol{a}_1$, $N_2\boldsymbol{a}_2$, $N_3\boldsymbol{a}_3$). The N_is are

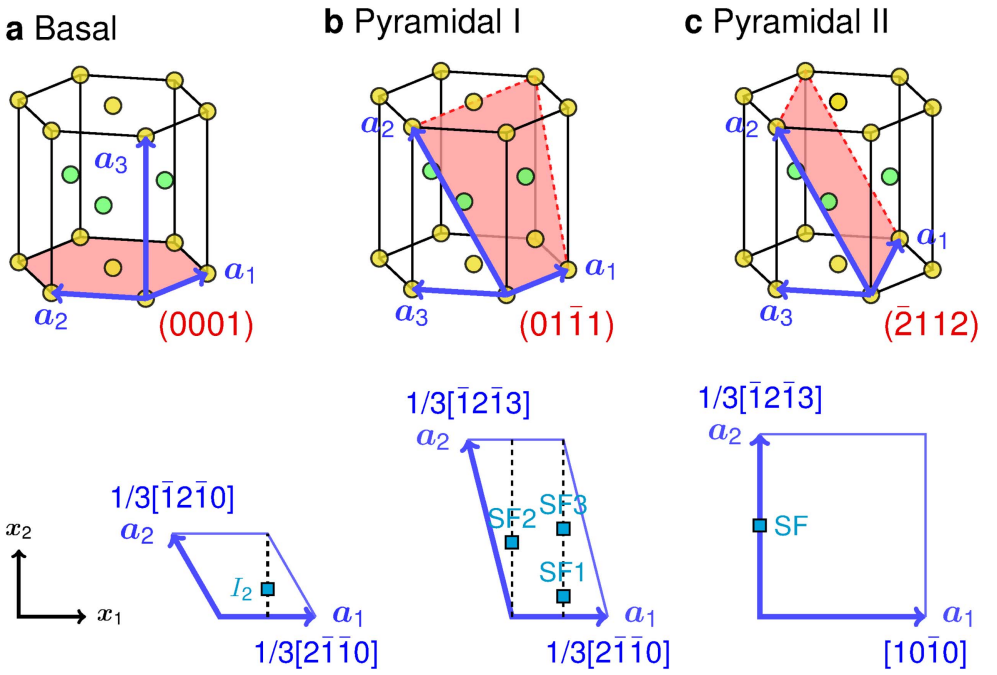

Figure 2. Schematic representation of coordinate system used in the simulation, and (a) basal, (b) pyramidal I, (c) pyramidal II slip planes along with positions of stable stacking faults observed.

chosen large enough such that periodic solute–solute interactions are negligible in order to remain in the limit of dilute concentrations.

We consider the intrinsic basal I_1 and the extrinsic E stacking faults neither of which can be generated by slip processes, and the intrinsic basal I_2, pyramidal I, and pyramidal II faults that are formed by slip processes. Simulation cells for the basal I_1 and E stacking faults are constructed by arranging close-packed basal planes as $(AB)_{N_3/2}$-$(AC)_{N_3/2}$ and $(AB)_{N_3/2}$-C-$(AB)_{(N_3-2)/2}$-C, respectively, where A, B and C are the stacking sequence of close-packed (111) planes in fcc crystals (ABCABC...) and basal planes (0001) in hcp crystals (ABAB...). As shown in figure 3(a), two such stacking faults are generated in each simulation box because of the periodic boundary condition used. The relaxed structures of these stacking faults are obtained by relaxing the simulation cell only in direction $\boldsymbol{x}_3$ normal to the fault plane. The slip stacking faults are generated using the tilted-box method [49] in which the simulation cell vector $N_3\boldsymbol{a}_3$ is shifted laterally by the stacking fault vector $\boldsymbol{t}$, as depicted in figure 3(b). Relaxation of the simulation cell is subject to $\sigma_{i3} = 0$ $(i = 1, 2, 3)$ while holding the $N_1\boldsymbol{a}_1$ and $N_2\boldsymbol{a}_2$ repeat vectors fixed. The in-plane positions of the various stable stacking faults are depicted in figure 2. An important advantage of the tilted-box method is that it allows full relaxation of all atoms, in contrast to solely out of stacking fault plane relaxation in the conventional method. The tilted-box method yields only stable stacking faults, if they exists, in the corresponding stacking fault plane.

To measure the solute/stacking fault interaction energies, we start with the corresponding relaxed stacking fault structure in the pure Mg. One Mg is then replaced by one Y solute atom

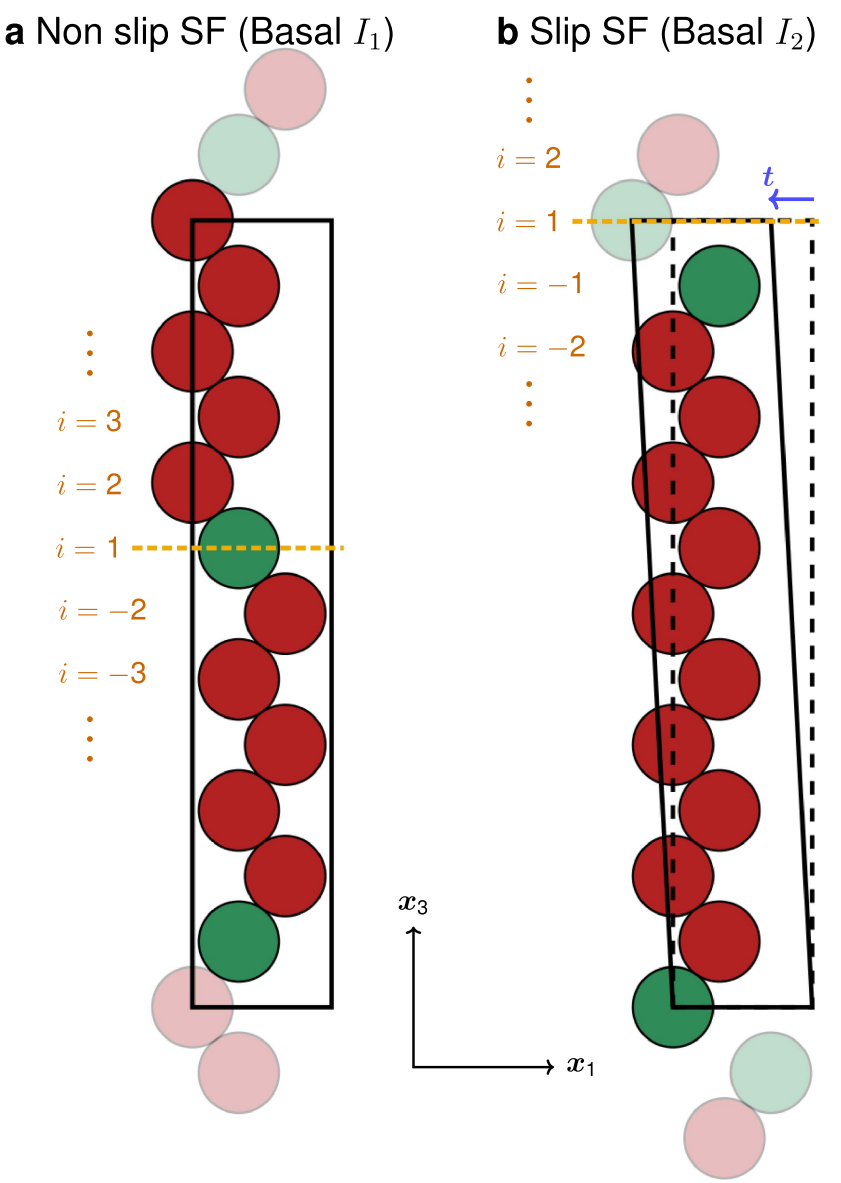

Figure 3. Schematics of the stacking fault simulation cells. (a) Basal I_1 stacking fault as a representative non-slip stacking fault. (b) Basal I_2 stacking fault as an example using the tilted-box method for creating slip stacking faults. In (b), the solid black lines denotes the initial simulation cell of perfect Mg and the dashed lines show the simulation box tilted by the stacking fault vector $\boldsymbol{t}$, leading to the formation of stacking fault. Index i refers to the solute position with respect to the stacking fault plane. Red and green atoms denote the hcp and fcc atoms, respectively.

at each unique atomic position at height r_i with respect to stacking fault plane as shown in figure 3. The simulation box is then relaxed only in the out-of-plane $\boldsymbol{x}_3$ direction; this prevents motion of the stacking fault. The interaction energy $E_{\text{int}}(r_i)$ of a solute at distance r_i from the stacking fault plane is then computed as

$$E_{\text{int}}(r_i) = (E_{\text{SF}}^{\text{A}} - E_B^{\text{A}}) - (E_{\text{SF}}^{\text{Mg}} - E_{\text{B}}^{\text{Mg}}), \tag{4}$$

where E_{SF}^{A} and $E_{\text{SF}}^{\text{Mg}}$ are the energies of the alloy (one Y atom at r_i from stacking fault) and pure Mg with the stacking fault, respectively. Note that these energies are total energies, not energies per unit area. E_{B}^{A} and E_{B}^{Mg} are the energies of the hcp structure with and without the Y solute, respectively. During the calculation of E_{B}^{A}, one Mg atom is replaced by one Y atom in the hcp bulk Mg and simulation box is then relaxed only in the out of corresponding stacking fault plane direction while keeping the in-plane repeat vectors fixed.

4.3.2. Stacking fault energies versus solute concentration. In the dilute limit (neglecting solute–solute interaction), we use the interaction energies to calculate the average stacking fault energy γ^{A} (energy per unit area) in the alloy as follows. For volume concentration $c \ll 1$ of solute, which is also equal to the planar concentration for a uniform random distribution of solutes in the material, the average stacking fault energy of the alloy γ^{A} can be written as

$$\gamma^{\text{A}} = \gamma^{\text{Mg}} + \frac{c}{A_0} \sum_{i=-\infty}^{\infty} E_{\text{int}}(r_i), \tag{5}$$

where γ^{Mg} is the stacking fault energy in the pure Mg and A_0 is the effective atomic area of one Mg atom corresponding to the stacking fault plane. Equation (5) can be written as

$$\gamma^{\text{A}} = \gamma^{\text{Mg}} + kc, \tag{6}$$

where $k = (\sum_{i=-\infty}^{\infty} E_{\text{int}}(r_i))/A_0$ is the coefficient characterizing the effects of solutes on the the stacking fault energy.

The interactions of Y atoms versus position for each of the the stable basal (I_1, I_2 and E), pyramidal I (SF2 and SF3), and pyramidal II stacking faults in Mg are shown in figure 4. Also shown are the DFT results of Yin *et al* [19] that were used for fitting of the MEAM Mg–Y potential. Also shown in each figure is the coefficient k as computed using the MEAM potential and DFT. For all planes, the interaction between a Y atom and the stacking fault becomes negligible after a few atomic layers from stacking fault plane. For basal stacking faults, the MEAM energies are always negative (attraction) whereas the DFT energies are negative for the first few planes but then become positive at larger distances. The basal intrinsic I_1, I_2 and extrinsic E stacking fault energies decrease with Y concentration but the MEAM potential yields k values that are approximately 50% smaller than the DFT results. The Y interactions with the pyramidal I SF2 show the same alternation in sign with positions in alternate layers, consistent with the variations in out-of-plane atomic relaxation in successive atomic layers in pure Mg [49]. But the MEAM values are again smaller in magnitude than the DFT values, leading to a smaller value of the coefficient k. There are no DFT results for the basal E and pyramidal I SF3 stacking faults. The Y interactions with the pyramidal II stacking fault are in reasonably good agreement with the DFT results in trend and magnitude. However, the MEAM value in the first plane is somewhat lower than the DFT value. This leads to a value for the coefficient k that is slightly smaller than, but comparable to, the DFT value. The MEAM and DFT values of k for the various stacking faults are shown again in table 6 along with the predictions of the Kim potential. The new MEAM potential is generally more accurate than the Kim potential in terms of signs and magnitudes, especially for the pyramidal I faults.

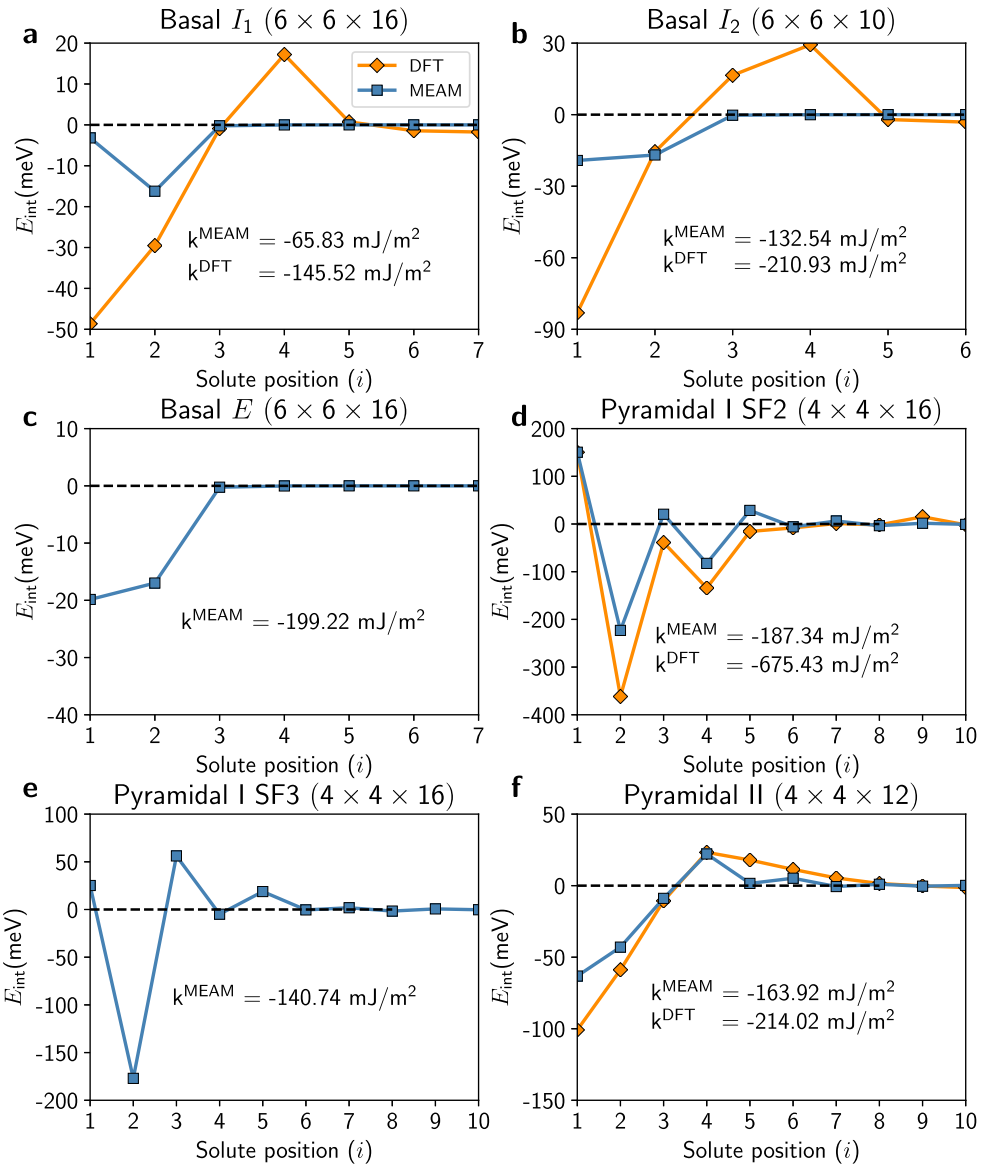

Figure 4. Interaction energy of Y with various stacking faults in Mg, as computed using the current MEAM potential and using DFT [19], as a function of distance from stacking fault plane: (a) basal I_1, (b) basal I_2, (c) basal E, (d) pyramidal I SF2, (e) pyramidal I SF3, and (f) pyramidal II. Size of the simulation cell $N_1 \times N_3 \times N_3$ for the corresponding stacking fault, used in MEAM calculation, is indicated in parentheses.

5. Y interactions with the pyramidal II $\langle \boldsymbol{c} + \boldsymbol{a} \rangle$ edge dislocation

Slip of $\langle \boldsymbol{c} + \boldsymbol{a} \rangle$ dislocations in Mg is crucial for achieving plastic strain in the $\langle \boldsymbol{c} \rangle$ direction. This motivated a recent DFT study of the interaction of Y solutes with the pyramidal II $\langle \boldsymbol{c} + \boldsymbol{a} \rangle$ edge dislocation core [50].

Table 6. Properties of Y solute atom in Mg as calculated by the current MEAM potential, DFT, and the Kim potential. $\Delta V/V_0$ is the normalized Y misfit volume of Y and k is coefficient for the average effect of solute concentration on the stacking fault energy (units of mJ m^{-2}).

	MEAM	Kim potential	DFT
$\Delta V/V_0$	0.593	0.240	0.567[a], 0.580[b], 0.636[c]
k(basal I_1)	−65.83	−2.41	−145.52[a]
k(basal I_2)*	−132.54	−5.33	−210.93[a]
k(basal E)	−199.22	−8.26	
k(pyramidal I SF2)*	−187.34	−19.08	−675.43[a]
k(pyramidal I SF3)	−140.74	73.32	
k(pyramidal II)*	−163.92	−250.45	−214.02[a]

Note: asterisks (*) denote the properties used during the potential fitting procedure.
[a] Yin *et al* [19].
[b] Sandlöbes *et al* [14].
[c] Yasi *et al* [48].

In DFT study, the simulation box has a periodic length of ∼1 nm along the line direction [50]. The computation yields the total energy $E_{\text{tot}}(x_{i,1}, x_{i,2})$ of the DFT cell containing the Mg dislocation and a solute at position $(x_{i,1}, x_{i,2})$ relative to the center of the dislocation core. The interaction energy is the difference between the solute at $(x_{i,1}, x_{i,2})$ and the reference energy E_{ref} of a solute far from the dislocation in the perfect crystal Mg lattice, $E_{\text{int}}(x_{i,1}, x_{i,2}) = E_{\text{tot}}(x_{i,1}, x_{i,2}) - E_{\text{ref}}$. Due to the small size of the DFT computational cell, it is not possible to compute E_{ref} in the same geometry. Uncertainties in the total energy computation also make it inaccurate to use a separate simulation of a solute in a periodic perfect crystal as the reference energy. A reference energy is therefore estimated by averaging the energies of the dislocation with solutes at all sites on the two planes on either side of the dislocation slip plane, $E_{\text{ref}} = (1/N)\sum_i E_{\text{tot}}(x_{i,1}, x_{i,2})$. For interaction energies governed only by the elastic interaction between the edge dislocation pressure field p and the solute misfit volume ΔV, $E_{\text{int}}(x_{i,1}, x_{i,2}) = p(x_{i,1}, x_{i,2})\ \Delta V$, the sum above should be nearly zero. Consistency of the estimated value of E_{ref} and the DFT results can be further assessed by comparing the DFT energies to the elasticity predictions for atomic sites away from the core, where the elasticity prediction becomes increasingly accurate and the field of interaction energies versus atomic position should be smooth. The use of the short periodic length combined with the low Peierls stress of the dislocation (and presumably of the individual partial dislocations) also leads to an inability to measure the interaction energy $E_{\text{int}}(x_{i,1}, x_{i,2})$ at sites whose neighbors along the glide plane have much lower (more negative) interactions. When a solute is placed in such a site, one or both partials glide such that the solute position relative to the dislocation core is in the energetically favorable site.

Simulation of the dislocation using the MEAM potential follows a standard method. We start with a large pure Mg simulation cell ($l_{x_1} \times l_{x_2} \times l_{x_3} \sim 30\ \text{nm} \times 30\ \text{nm} \times 1\ \text{nm}$) with $\boldsymbol{x}_1$–$\boldsymbol{x}_3$ as the glide plane, $\boldsymbol{x}_3$ axis parallel to the dislocation line, and $\boldsymbol{x}_2$ axis normal to the glide plane. A straight dislocation is introduced at the origin by applying the anisotropic elastic displacement field [11] corresponding to the Volterra dislocation. Relaxation of atomic positions is then carried out while holding fixed those atoms within two times the cutoff radius ($2r_c$) from the outer boundary. Periodic boundary conditions are used in the dislocation line direction. Relaxation is performed using the conjugate gradient method until the forces on

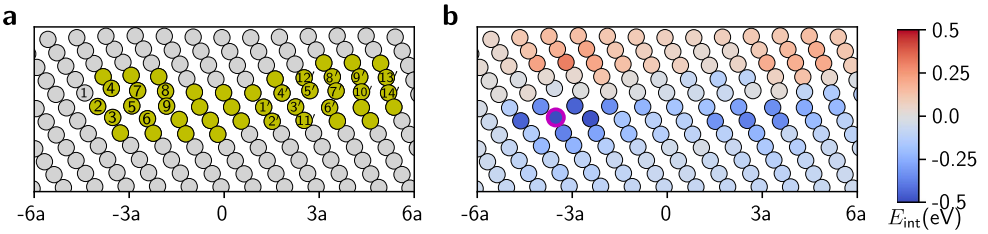

Figure 5. (a) Core structure of pyramidal II $\langle \boldsymbol{c} + \boldsymbol{a} \rangle$ edge dislocation in pure Mg obtained from MEAM potential. Yellow atoms correspond to non-hcp core atoms as identified from common neighbor analysis. Atomic sites are marked for which interaction energies are listed in table 7. (b) Interaction energy map for different atomic sites around the dislocation with $l_{x_3} \sim 6.5$ nm, as computed from the MEAM potential. For the site highlighted by the cyan outline, the interaction energy of −0.563 eV is beyond the range of the indicated scale.

all atoms are less than 10^{-6} eV Å^{-1}. A single-solute is then introduced at $(x_{i,1}, x_{i,2})$, the system is relaxed and the total energy is computed. The interaction energy is then computed as $E_{\text{int}}(x_{i,1}, x_{i,2}) = E_{\text{tot}}(x_{i,1}, x_{i,2}) - E_{\text{ref}}$. Here, E_{ref} can be computed either by placing a solute far from the dislocation (but not near the outer boundary) or in a separate perfect crystal simulation. As in the DFT simulations, high energy solute sites are not always measurable because the dislocation can glide such that the solute resides in a lower energy site relative to the final position of the dislocation. In atomistic simulations, which are not limited to small sizes, this issue can sometimes be mitigated by using a longer dislocation line length. However, for longer line lengths, the dislocation may still glide locally near the solute while remaining in the original locations further away, i.e. the dislocation becomes bowed. Thus, the computed energy may still not reflect the true interaction energy of a solute with a straight dislocation.

The interaction energies of Y solutes for all of the atomic sites around the edge dislocation as computed using the Mg–Y MEAM potential are shown in figure 5(b) for dislocation line length ∼6.5 nm. Specific MEAM and DFT values for the sites shown in figure 5(a) are listed in table 7. The table indicates those sites that are unstable, and the final relative position of the solute due to dislocation glide during relaxation. MEAM computations are carried out for two lengths, $l_{x_3} \sim 1$, 6.5 nm. For cases where solutes are stable at both lengths, the difference reflects solute–solute interactions at a separation ∼1 nm. For cases where the solutes are unstable at $l_{x_3} \sim 1$ nm, the energies at $l_{x_3} \sim 6.5$ nm are estimates only due to possible dislocation bowing.

The interaction energies calculated from the MEAM potential with $l_{x_3} \sim 6.5$ nm are generally in good agreement with the DFT values. The sign of interaction energies—indicating the attractive and repulsive sites—at each site are same in both DFT and MEAM calculations except for the site 4. Moreover, in both DFT and MEAM calculations, the most stable sites around both partials (site 3 around left partial and site 6′ around right partial) are the same. In DFT, site number 7′ has a very large positive interaction energy which is unusual given that the neighboring sites (4′, 10′) have negative interaction energies and so the dislocation would be expected to glide to one of these substantially lower-energy sites. The typical absolute deviation in interaction energy, excluding sites 4 and 7′, is ∼0.04 eV, with a maximum of 0.107 eV for site 2′. The absence of any systematic difference suggests that the reference energy used in the DFT is reasonable. The deviations also might not be crucial

Table 7. Interaction energy, in eV, of Y with the pyramidal II $\langle \boldsymbol{c} + \boldsymbol{a} \rangle$ edge dislocation in Mg at various atomic sites around the dislocation core, as calculated from the current MEAM potential and using DFT. The atomic sites of Y solute are marked in figure 5(a).

Site#	Interaction energy (eV)			Site#	Interaction energy (eV)		
	MEAM		DFT		MEAM		DFT
	$l_{x_3} \sim 1$ nm	$l_{x_3} \sim 6.5$ nm	$l_{x_3} \sim 1$ nm		$l_{x_3} \sim 1$ nm	$l_{x_3} \sim 6.5$ nm	$l_{x_3} \sim 1$ nm
1	$*(\rightarrow 4)$	0.034	0.081	$1'$	$*(\rightarrow 6')$	−0.187	−0.211
2	$*(\rightarrow 5)$	−0.344	*	$2'$	$*(\rightarrow 11')$	−0.327	−0.220
3	−0.558	−0.563	−0.475	$3'$	$*(\rightarrow 6')$	−0.289	−0.278
4	−0.056	−0.033	0.180	$4'$	−0.095	−0.068	−0.090
5	−0.445	−0.446	−0.385	$5'$	$*(\rightarrow 4')$	−0.011	*
6	$*(\rightarrow 3)$	−0.482	*	$6'$	−0.333	−0.340	−0.280
7	$*(\rightarrow 4)$	−0.003	*	$7'$	$*(\rightarrow 4')$	0.022	1.183
8	0.043	0.017	0.054	$8'$	$*(\rightarrow 12')$	0.074	0.048
9	−0.341	−0.342	−0.308	$9'$	$*(\rightarrow 13')$	0.135	0.074
				$10'$	$*(\rightarrow 14')$	−0.099	−0.074
				$11'$	−0.384	−0.376	
				$12'$	−0.111	−0.112	
				$13'$	0.047	0.042	
				$14'$	−0.147	−0.151	

Note: asterisks(∗) mean that the dislocation configuration is unstable for solutes at that site, and the dislocation partial glides to put the solute on the site mentioned in parentheses.

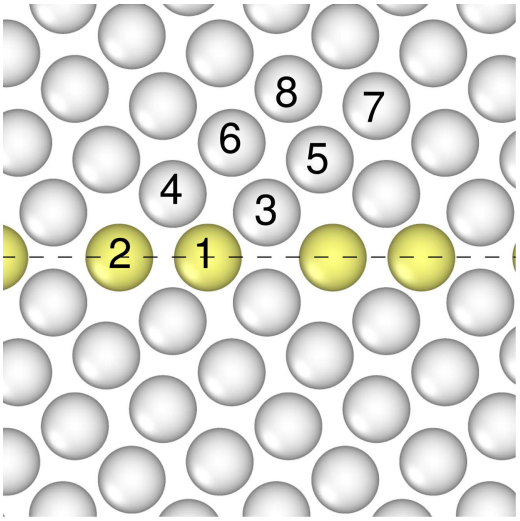

Figure 6. Structure of the $\{10\bar{1}2\}\langle\bar{1}011\rangle$ tension-twin boundary in pure Mg as calculated using the MEAM potential. White atoms, identified using common neighbor analysis, represent hcp atoms while yellow atoms correspond to non-hcp atoms. The marked sites show the positions of solute with respect to the twin boundary for which the interaction energies are tabulated in table 8.

because dislocation properties are influenced by the collective solute field in a random alloy [51]. Finally, the interactions of Y with the left partial dislocation (around $x_1 = -3a$ in figure 5(b)) are observed to be stronger than around the right partial dislocation (at around $x_1 = 3a$ in figure 5(b)), which is consistent with the wider spreading of the right partial dislocation core. The wider spreading of right partial core is also presumably associated with a lower Peierls stress that leads to a larger number of atomic sites being unstable to glide that partial.

6. Y interaction with $\{10\bar{1}2\}\langle\bar{1}011\rangle$ tension-twin boundary

In pure Mg, the $(10\bar{1}2)$ tension-twin is the most dominant twin mode for accommodation of $\boldsymbol{c}$-axis plastic strain under $\boldsymbol{c}$-axis tension [52, 53]. Therefore, the interaction energy of Y solutes with the twin boundary—which dictates the strengthening of twinning dislocations [54]—is calculated here with the MEAM potential and compared to DFT values for various positions of the Y solute.

We create the coherent twin boundary starting from Mg bulk hcp simulation box having periodic boundary condition in all directions following the methodology in Ghazisaeidi *et al* [54]. $\boldsymbol{x}_1$ and $\boldsymbol{x}_2$ axes of the simulation box lie in the twin plane $(10\bar{1}2)$ with $\boldsymbol{x}_1$ axis along the twinning direction $[\bar{1}011]$, and the $\boldsymbol{x}_3$ axis perpendicular to the twin plane. The simulation box contains 5120 Mg atoms and has dimensions ~60 Å × 25 Å × 74 Å. The twin boundary is constructed by applying mirror symmetry on the bulk Mg hcp lattice across the twin plane followed by relaxation of all atomic positions and simulation box dimension perpendicular to the twin boundary to forces below 10^{-6} meV Å^{-1}. After relaxation, two coherent twin boundaries are formed separated by 24 atomic layers, as shown in figure 6 and in good agreement with the DFT-computed structure [52, 54]. The

Table 8. Interaction energy, in eV, of Y solutes with the $\{10\bar{1}2\}\langle\bar{1}011\rangle$ tension-twin in Mg, as calculated from the current MEAM potential and DFT. The atomic sites are indicated in figure 6. Migration of the twin boundary is observed in DFT calculation for one solute at site 6 and so the quoted value is derived from a DFT containing two symmetric solutes in sites 6 (see text).

Site#	Interaction energy (eV)		Site#	Interaction energy (eV)	
	MEAM	DFT		MEAM	DFT
1	0.342 9	0.2269	5	0.0600	0.0784
2	−0.3162	−0.2639	6	−0.0783	−0.0998*
3	0.0291	−0.0213	7	0.0001	−0.0119
4	0.0341	−0.0004	8	−0.0172	0.0180

twin boundary energy using the current MEAM potential is 149 mJ m^{-2}, somewhat higher than the DFT values of 114 mJ m^{-2} [52, 54, 55] and 118 mJ m^{-2}[56].

We calculate the interaction energy of Y solute atoms at the positions shown in the figure 6 following the methodology described in section 5 for the calculation of pyramidal II $\langle \mathbf{c} + \boldsymbol{a} \rangle$ edge dislocation-Y solute interaction energy. The reference energy E_{ref} is calculated as the Y energy at an atomic site situated in the bulk-equivalent site halfway between the two twin boundaries. A Y atom is substituted into each atomic site and the total energy $E_{\text{tot}}(i)$ is computed, from which the interaction energy is computed as $E_{\text{int}}(i) = E_{\text{tot}}(i) - E_{\text{ref}}$. The same steps are followed for both MEAM and DFT calculations and the interaction energies thus obtained are listed in table 8. Sites 1 and 2 are the prominent compression and dilatation sites, respectively, and so show large interaction energies. The MEAM potential yields stronger interactions as compared to the DFT. The interaction energy decays rapidly with distance from the twin boundary, justifying the calculated reference energy.

In the DFT calculation, the twin boundary is observed to migrate when a Y atom is introduced at site 6, making the interaction energy calculation impossible. To circumvent the migration, two solutes are introduced at two symmetric sites 6, one above the twin plane and other below. The two symmetric solutes prevent boundary migration. Assuming no interaction between the two solutes, the interaction energy is one-half the interaction energy of the structure with two solutes minus the energy of a reference structure. This yields an interaction energy for site 6 that is negative and relatively large compared to the neighboring sites. This would then suggest that a solute at site 6 is quite stable, whereas the DFT shows that the boundary migrates for a solute at just one site 6; this issue is not understood at this time. Using the MEAM potential, two solutes at two symmetric sites 6 yields an interaction energy of −0.0776 eV quite close to the value of −0.0783 eV for one solute at site 6, suggesting the absence of elastic interactions between the two solutes. Finally, sites 3 and 4 have positive interaction energies in the MEAM potential calculation while DFT yields negative interaction energies, but the absolute energies are fairly small. Overall, the agreement between DFT and MEAM potential is not highly accurate but the MEAM potential may still provide qualitative understanding of solute effects on twin deformation in Mg–Y alloys.

7. Discussion

The Mg–Y MEAM potential developed here starts with the constituent MEAM potentials for Mg (Wu *et al* [5]) and, with slight modifications, Y (Ko and Lee [30], Kim *et al* [21]). The additional potential parameters corresponding to binary Mg–Y are fitted against the enthalpy of formation, lattice and elastic constants of the B2 Mg–Y intermetallic, and the interactions of Y solutes with the basal I_1, I_2, pyramidal I SF2, and pyramidal II stacking faults. The resulting potential provides the best overall fits to the target properties that we have been able to obtain across the range of MEAM parameters. The potential was then used to compute the properties of several other intermetallic compounds, the solute misfit volume, the solute interactions with the basal E and pyramidal I SF3 stacking faults (for which no DFT results exist), and the solute interactions with the pyramidal II $\langle \boldsymbol{c} + \boldsymbol{a} \rangle$ edge dislocation and with $\{10\bar{1}2\}\langle \bar{1}011 \rangle$ tension-twin boundary.

The potential makes predictions that are generally in reasonable agreement with experiments and/or DFT. However, as with all potentials, the agreement is not perfect. Since plastic deformation in Mg involves many different dislocation phenomena (solute strengthening of various slip systems, pyramidal-to-basal transformation, pyramidal cross-slip), it is thus important to carefully identify those problems for which the potential is useful and those problems where the potential remains insufficient for obtaining realistic semi-quantitative results.

First, the MEAM solute misfit volume is well-captured. This is important for solute interactions with the pressure field of a dislocation. These interactions tend to dominate solute strengthening [48, 51, 57]. The role of the solute interaction with the basal I_2 stacking fault in solute strengthening of basal slip appears small [58], suggesting that the potential is suitable for the study of basal solute strengthening. The full interactions with the pyramidal II $\langle \boldsymbol{c} + \boldsymbol{a} \rangle$ edge dislocation around the core are also reasonably good (with the exception of one unusual site energy in the DFT results). Along with the good misfit volume, this indicates that the potential should be suitable for semi-quantitative assessment of pyramidal II solute strengthening. Together, these enable some assessment of the plastic anistropy as characterized by the ratio of pyramidal II to basal Peierls stresses. The interactions of Y with the pyramidal I $\langle \boldsymbol{c} + \boldsymbol{a} \rangle$ and prismatic $\langle \boldsymbol{a} \rangle$ dislocations have not been examined, and so applications to strengthening of these slip systems is not yet validated.

The solute interactions with the pyramidal II stacking fault are also well-captured. This is encouraging since pyramidal II $\langle \boldsymbol{c} + \boldsymbol{a} \rangle$ dislocations are energetically preferred to pyramidal I $\langle \boldsymbol{c} + \boldsymbol{a} \rangle$ dislocations, such that study of pyramidal II $\langle \boldsymbol{c} + \boldsymbol{a} \rangle$ is probably more important than study of pyramidal I $\langle \boldsymbol{c} + \boldsymbol{a} \rangle$. The MEAM solute interactions with the basal faults are reasonable, but not quite strong enough. The resulting k values are then too small in comparison to the corresponding value for the pyramidal II stacking fault. This suggests some inaccuracy in using the potential to examine the pyramidal-to-basal $\langle \boldsymbol{c} + \boldsymbol{a} \rangle$ transformation of the pyramidal II edge dislocation. However, at low solute concentrations the absolute difference in basal stacking fault energy will be small and the pyramidal-to-basal transition is not dominated by the energy of the I_1 stacking fault [59]. Thus, the potential may provide some insights into any role of Y solutes in modifying the energy barrier for this transformation [20].

The interaction energy of Y solute atoms with the $\{10\bar{1}2\}\langle \bar{1}011 \rangle$ tension-twin boundary is in reasonable agreement with the DFT values. The prominent interacting sites within the twin boundary interface are accurately identified but have a stronger interaction energy than found in DFT. These highly interacting sites are important for solute segregation along twin boundary, which can control the strength of Mg alloys after annealing [60]. Due to some differences in the interaction energies, the strengthening of the twinning dislocation might not

be computed with high accuracy but the potential can be utilized for qualitative assessment of the strengthening effects of Y.

The major deviation for the MEAM potential is in the value of k for the pyramidal I SF2 stacking fault. The MEAM potential predicts this value to be comparable to the k value for pyramidal II, whereas the DFT value for the pyramidal I k is approximately 3 times larger than that of pyramidal II. The MEAM potential therefore cannot be used to fully investigate the change in pyramidal II to pyramidal I cross-slip energy barrier, which we believe holds the key to understanding ductility in Mg alloys [16]. However, the potential can be used to assess the role of specific solute configurations in reducing the pyramidal II-I cross-slip barrier. Specifically, since the solute/stacking fault interactions at individual sites around the pyramidal II and pyramidal I faults can be computed with reasonable accuracy using the MEAM potential, the energies of pyramidal II and pyramidal I screw dislocations in the presence of specific solute configurations can be analyzed, and the cross-slip barrier between pyramidal II and pyramidal I computed. The correlation of local solute energies, even if approximate, with a corresponding change in cross-slip barrier would enable testing of assumptions underlying the model proposed by Wu *et al* [16].

The application of any interatomic potential must always be undertaken with care. Researchers may identify other valuable phenomena for which atomistic studies of Mg–Y could be insightful. The current potential may be useful for examining such problems, especially for testing mechanistic models. However, we advocate that researchers examine the properties of this Mg–Y potential in detail to validate, quantitatively or qualitatively, its applicability to any specific phenomenon. We also encourage further validation and testing of the potential to reveal any additional positive features or to expose any flaws that would make the potential unsuitable for certain problems. We will report on the application of this Mg–Y potential to the study of some of the above-mentioned problems in future work.

Acknowledgments

RA and WAC acknowledge financial support of this work through a grant from the Swiss National Science Foundation entitled ‘Control of Atomistic Mechanisms of Flow in Magnesium Alloys to Achieve High Ductility’ (project #162350). The authors thank Dr Binglun Yin for providing the DFT analysis of Y–Y solute interaction energies.

Appendix. Formalism of MEAM interatomic potential

Here we present the theory behind the MEAM interatomic potential following Lee and Baskes [28] and Lee *et al* [29].

A.1. Formalism for pure element

Under the framework of MEAM potential, energy of a system is given as

$$E = \sum_i \left[F(\bar{\rho}_i) + \frac{1}{2} \sum_{j(\neq i)} \phi_{ij}(R_{ij}) \right], \tag{A.1}$$

where F is the embedding function, $\bar{\rho}_i$ is the background electron density at site i, ϕ_{ij} is the pair interaction between atoms at sites i and j with a distance R_{ij} between them. The embedding function takes the form

$$F(\bar{\rho}) = AE_c \frac{\bar{\rho}}{\bar{\rho}^0} \ln \frac{\bar{\rho}}{\bar{\rho}^0}, \tag{A.2}$$

where A is an element-dependent adjustable parameter, E_c is the cohesive energy, and $\bar{\rho}^0$ is the background electron density for a reference structure which is usually the equilibrium structure. The background electron density $\bar{\rho}_i$ comprised spherically symmetric partial contribution $\rho_i^{(0)}$ and angular partial contributions $\rho_i^{(1)}$, $\rho_i^{(2)}$ and $\rho_i^{(3)}$, which are expressed as

$$(\rho_i^{(0)})^2 = \left[\sum_{j(\neq i)} \rho_j^{a(0)}(R_{ij}) S_{ij}\right]^2, \tag{A.3a}$$

$$(\rho_i^{(1)})^2 = \sum_{\alpha} \left[\sum_{j(\neq i)} \frac{R_{ij}^{\alpha}}{R_{ij}} \rho_j^{a(1)}(R_{ij}) S_{ij}\right]^2, \tag{A.3b}$$

$$(\rho_i^{(2)})^2 = \sum_{\alpha,\beta} \left[\sum_{j(\neq i)} \frac{R_{ij}^{\alpha} R_{ij}^{\beta}}{R_{ij}^2} \rho_j^{a(2)}(R_{ij}) S_{ij}\right]^2 - \frac{1}{3}\left[\sum_{j(\neq i)} \rho_j^{a(2)}(R_{ij}) S_{ij}\right]^2, \tag{A.3c}$$

$$(\rho_i^{(3)})^2 = \sum_{\alpha,\beta,\gamma} \left[\sum_{j(\neq i)} \frac{R_{ij}^{\alpha} R_{ij}^{\beta} R_{ij}^{\gamma}}{R_{ij}^3} \rho_j^{a(3)}(R_{ij}) S_{ij}\right]^2 - \frac{3}{5}\sum_{\alpha} \left[\sum_{j(\neq i)} \frac{R_{ij}^{\alpha}}{R_{ij}} \rho_j^{a(3)}(R_{ij}) S_{ij}\right]^2, \tag{A.3d}$$

where $\rho_j^{a(h)}(R_{ij})$ denote the atomic electron densities from a site j at a distance R_{ij} from site i, R_{ij}^{α} is the α component of distance vector between atoms at sites j and i, and S_{ij} is the screening between atoms at sites i and j as described below. Several expressions have been proposed to combine the partial electron densities to obtain the total background electron density [61]. We use the following expression in the present work

$$\bar{\rho}_i = \rho_i^{(0)} G(\Gamma_i), \tag{A.4a}$$

$$G(\Gamma) = \frac{2}{1 + \exp(-\Gamma)}, \tag{A.4b}$$

$$\Gamma_i = \sum_{h=1}^{3} t^{(h)} \left[\frac{\rho_i^{(h)}}{\rho_i^{(0)}}\right]^2, \tag{A.4c}$$

where $t^{(h)}$ are adjustable parameters. The atomic electron density is computed as

$$\rho_j^{a(h)}(R_{ij}) = \rho_0 \exp\left[-\beta^{(h)}\left(\frac{R_{ij}}{r_e} - 1\right)\right], \tag{A.5}$$

where ρ_0 is element-dependent density scaling factor, $\beta^{(h)}$ are adjustable parameters, and r_e is the nearest-neighbor distance in the equilibrium reference structure.

After determining the embedding function, we turn our attention to the pair potential contribution $\phi(R)$ in the total energy given by equation (A.1). In MEAM, no specific functional form is given to pair potential $\phi(R)$, instead, it is determined from the known values of total energy and embedding function. The energy per atom for the reference structure is obtained from the universal equation of state by Rose *et al* [31] as a function of nearest-neighbor R

$$E^u(R) = -E_{ic}(1 + a^* + da^{*3})\exp(-a^*), \tag{A.6a}$$

$$a^* = \alpha\left(\frac{R}{r_e} - 1\right), \tag{A.6b}$$

$$\alpha = \sqrt{\frac{9B\Omega}{E_c}}, \tag{A.6c}$$

where d is an adjustable parameter, B is the bulk modulus, and Ω is equilibrium atomic volume. Considering the second-nearest-neighbor interaction, energy per atom in the reference structure is written by using equation (A.1)

$$E^u(R) = F[\bar{\rho}(R)] + \frac{Z_1}{2}\phi(R) + \frac{Z_2 S}{2}\phi(aR), \tag{A.7}$$

where $\bar{\rho}(R)$ is the background electron density, Z_1 and Z_2 are, respectively, number of the first and second-nearest-neighbor atoms, a is the ratio between the second and first nearest-neighbor distance, and S is the screening on the second-nearest-neighbor interaction. Another function $\psi(R)$ is introduced to write equation (A.7) as

$$E^u(R) = F[\bar{\rho}(R)] + \frac{Z_1}{2}\psi(R), \tag{A.8a}$$

$$\psi(R) = \phi(R) + \frac{Z_2 S}{Z_1}\phi(aR). \tag{A.8b}$$

Now, $\psi(R)$ can be calculated as a function of R from equation (A.8a) and then, $\phi(R)$ is computed as function of R by using following relation

$$\phi(R) = \psi(R) + \sum_{n=1}(-1)^n\left(\frac{Z_2 S}{Z_1}\right)^n \psi(a^n R), \tag{A.9}$$

where summation is performed until the correct value of energy is obtained.

Now we discuss the final component of elemental-MEAM potential, the screening function S_{ij} between the atoms at sites i and j. Screening function is built such that $S_{ij} = 1$ for completely unscreened atoms within the cutoff radius r_c of the potential, and $S_{ij} = 0$ for atom pair completely screened or outside the cutoff radius. For partial screening, it takes a value between 0 and 1. The total screening function is the product of the radial cutoff function and three body terms The expression for screening function is

$$S_{ij} = \bar{S}_{ij} f_c\left(\frac{r_c - R_{ij}}{\Delta r}\right), \tag{A.10a}$$

$$\bar{S}_{ij} = \prod_{k(\neq i,j)} S_{ikj}, \tag{A.10b}$$

$$f_c(x) = \begin{cases} 1 & x \geqslant 1, \\ [1 - (1 - x)^4]^2 & 0 < x < 1, \\ 0 & x \leqslant 0, \end{cases} \tag{A.10c}$$

where Δr is parameter to smoothen the radial cutoff of potential which has a cutoff radius r_c. Three body screening function S_{ikj}, amount of screening between atoms at i and j due to atom at k, is determined from a simple geometrical construction. Imagine an ellipse in $\boldsymbol{x}$–$\boldsymbol{y}$ plane passing through atoms i, j and k with the atoms i and j on the $\boldsymbol{x}$ axis

$$x^2 + \frac{y^2}{C} = \left(\frac{R_{ij}}{2}\right)^2, \tag{A.11}$$

where the value of C is computed for every atom k. Two adjustable limiting values $C_{\min}$ and $C_{\max}$ ($C_{\max} > C_{\min}$) are defined for every possible triplet (i, j, k). If atom k is located outside the ellipse defined by $C_{\max}$, that is , $C > C_{\max}$, the atom k does not provide any screening. If atom k is inside the ellipse defined by $C_{\min}$, that is, $C < C_{\min}$, the atom k completely screens the interaction between i and j. On the other hand, if $C_{\min} < C < C_{\max}$, there will be only partial screening. Following is the expression for three body screening function S_{ikj} which satisfies the conditions mentioned above

$$S_{ikj} = f_c\left(\frac{C(i,\,k,\,j) - C_{\min}(i,\,k,\,j)}{C_{\max}(i,\,k,\,j) - C_{\min}(i,\,k,\,j)}\right), \tag{A.12}$$

$$C(i,\,k,\,j) = 1 + \frac{2(R_{ij}^2 R_{ik}^2 + R_{ij}^2 R_{jk}^2 - R_{ij}^4)}{R_{ij}^4 - (R_{ik}^2 - R_{jk}^2)^2}. \tag{A.13}$$

A.2. Formalism for binary system

Interatomic potential of binary system, under MEAM framework, is constructed upon the potential of individual constituents. In addition to individual elements, pair interaction between different elements is required. Considering an ordered binary intermetallic as the reference structure (here we assume having $\frac{1}{2}i$ atom + $\frac{1}{2}j$ atom), the total energy per atoms $E_{ij}^u(R)$ as a function of nearest-neighbor distance R is given as

$$E_{ij}^u(R) = \frac{1}{2}\left[F_i(\bar{\rho}_i) + F_j(\bar{\rho}_j) + Z_1^{ij}\phi_{ij}(R) + \frac{1}{2}Z_2^{ij}\{S_i\phi_{ii}(aR) + S_j\phi_{jj}(aR)\}\right], \tag{A.14}$$

where E_{ij}^u is determined from the equation of state [31] using experimentally determined cohesive energy E_c, bulk modulus B, atomic volume Ω and parameter d. The embedding functions F_i and F_j can always be computed. Z_1^{ij} and Z_2^{ij} are, respectively, number of the first and second-nearest-neighbor atoms in the reference structure, ϕ_{ii} and ϕ_{ij} are pair interaction, respectively between i atoms and between j atoms, and a is the ratio between the second and first nearest-neighbor distances. Therefore, the pair interaction between the different types of atoms is calculated as

$$\phi_{ij}(R) = \frac{1}{Z_1^{ij}}\left[2E_{ij}^u(R) - F_i(\bar{\rho}_i) - F_j(\bar{\rho}_j) - \frac{1}{2}Z_2^{ij}\{S_i\phi_{ii}(aR) + S_j\phi_{jj}(aR)\}\right]. \tag{A.15}$$

The values of $C_{\max}$ and $C_{\min}$ are needed to be specified for all possible triplet of atom types. For pure elements, there is only one possible triplet, however, for binary system there are four possible types of triplet. Additionally, the density scaling factor ρ_0, see equation (A.5), also becomes important for binary alloys. This is an arbitrary value having no effect on the calculation for pure elements. However, for alloy systems, especially for systems where the constituent elements have different coordination numbers, the scaling factor (the ratio of the two values) has a great effect on calculations. In the current work, ρ_0, $C_{\min}$(Mg, Y, Mg), and $C_{\min}$(Y, Mg, Y) were used to correlate the elastic constants, and the interaction between Y and I2 stacking fault. In addition $C_{\min}$(Mg, Mg, Y) was set to 0 to qualitatively recover the trend on k between I2, pyramidal I SF2 and pyramidal II SF.

ORCID iDs

Rasool Ahmad https://orcid.org/0000-0002-4154-6902

References

[1] Friedrich H and Schumann S 2001 *J. Mater. Process. Technol.* **117** 276–81
[2] Kulekci M K 2008 *Int. J. Adv. Manuf. Technol.* **39** 851–65
[3] Staiger M P, Pietak A M, Huadmai J and Dias G 2006 *Biomaterials* **27** 1728–34
[4] Tonda H and Ando S 2002 *Metall. Mater. Trans.* A **33** 831–6
[5] Wu Z, Francis M F and Curtin W A 2015 *Modelling Simul. Mater. Sci. Eng.* **23** 015004
[6] Geng J, Chisholm M, Mishra R and Kumar K 2015 *Phil. Mag.* **95** 3910–32
[7] Obara T, Yoshinga H and Morozumi S 1973 *Acta Metall.* **21** 845–53
[8] Stohr J F and Poirier J P 1972 *Phil. Mag.* A **25** 1313–29
[9] Wu Z and Curtin W A 2016 *Scr. Mater.* **116** 104–7
[10] Wu Z and Curtin W A 2015 *Nature* **526** 62–7
[11] Anderson P M, Hirth J P and Lothe J 2017 *Theory of Dislocations* 3rd edn (New York: Cambridge University Press)
[12] Agnew S R, Senn J W and Horton J A 2006 *JOM* **58** 62–9
[13] Sandlöbes S, Zaefferer S, Schestakow I, Yi S and Gonzalez-Martinez R 2011 *Acta Mater.* **59** 429–39
[14] Sandlöbes S, Pei Z, Friak M, Zhu L F, Wang F, Zaefferer S, Raabe D and Neugebauer J 2014 *Acta Mater.* **70** 92–104
[15] Sandlöbes S, Friak M, Neugebauer J and Raabe D 2013 *Mater. Sci. Eng.* A **576** 61–8
[16] Wu Z, Ahmad R, Yin B, Sandlöbes S and Curtin W A 2018 *Science* **359** 447–52
[17] Agnew S R, Capolungo L and Calhoun C A 2015 *Acta Mater.* **82** 255–65
[18] Sandlöbes S, Friák M, Zaefferer S, Dick A, Yi S, Letzig D, Pei Z, Zhu L F, Neugebauer J and Raabe D 2012 *Acta Mater.* **60** 3011–21
[19] Yin B, Wu Z and Curtin W A 2017 *Acta Mater.* **136** 249–61
[20] Ahmad R, Wu Z, Groh S and Curtin W A 2018 *Scr. Mater.* **155** 114–8
[21] Kim K H, Jeon J B and Lee B J 2015 *Calphad* **48** 27–34
[22] Pei Z *et al* 2013 *New J. Phys.* **15** 043020
[23] Nogaret T, Curtin W A, Yasi J A, Hector L G and Trinkle D R 2010 *Acta Mater.* **58** 4332–3
[24] Plimpton S 1995 *J. Comput. Phys.* **117** 1–19
[25] Stukowski A 2010 *Modelling Simul. Mater. Sci. Eng.* **18** 015012
[26] Baskes M I 1987 *Phys. Rev. Lett.* **59** 2666–9
[27] Baskes M I 1992 *Phys. Rev.* B **46** 2727–42
[28] Lee B J and Baskes M I 2000 *Phys. Rev.* B **62** 8564–7
[29] Lee B-J, Baskes M, Kim H and Koo Cho Y 2001 *Phys. Rev.* B **64** 184102
[30] Ko W-S and Lee B-J 2009 *Acta Mater.* **57** 3140–7
[31] Rose J H, Smith J R, Guinea F and Ferrante J 1984 *Phys. Rev.* B **29** 2963–9
[32] Kittel C 2005 *Introduction to Solid State Physics* 8th edn (New York: Wiley)
[33] Spedding F H, Daane A H and Herrmann K W 1956 *Acta Crystallogr.* **9** 559–63
[34] Simmons G and Wang H 1971 *Single Crystal Elastic Constants and Calculated Aggregate Properties: a Handbook* (Cambridge, MA: MIT Press)
[35] Vitos L, Ruban A, Skriver H and Kollár J 1998 *Surf. Sci.* **411** 186–202
[36] Smith J, Bailey D, Novotny D and Davison J 1965 *Acta Metall.* **13** 889–95
[37] Zhang H, Shang S, Saal J E, Saengdeejing A, Wang Y, Chen L Q and Liu Z K 2009 *Intermetallics* **17** 878–85
[38] Zheng J, Tian X, Wei X L, Shao L, Pan X Z and Tang B Y 2015 *Mater. Chem. Phys.* **167** 70–6
[39] Chen G and Zhang P 2013 *Def. Technol.* **9** 131–9
[40] Chen Q, Huang Z, Zhao Z and Hu C 2013 *Comput. Mater. Sci.* **67** 196–202
[41] Ganeshan S, Shang S L, Zhang H, Wang Y, Mantina M and Liu Z K 2009 *Intermetallics* **17** 313–8
[42] Wang N, Yu W Y, Tang B Y, Peng L M and Ding W J 2008 *J. Phys. D: Appl. Phys.* **41** 195408
[43] Zeng M X, Tang B Y, Peng L M and Ding W J 2011 *Adv. Mater. Res.* **233–235** 2231–8
[44] Beckstein O, Klepeis J E, Hart G L W and Pankratov O 2001 *Phys. Rev.* B **63** 134112
[45] Bacon D J, Barnett D M and Scattergood R O 1980 *Prog. Mater. Sci.* **23** 51–262

[46] Clouet E, Garruchet S, Nguyen H, Perez M and Becquart C S 2008 *Acta Mater.* **56** 3450–60
[47] Varvenne C, Bruneval F, Marinica M C and Clouet E 2013 *Phys. Rev.* B **88** 1–7
[48] Yasi J A, Hector L G and Trinkle D R 2010 *Acta Mater.* **58** 5704–13
[49] Yin B, Wu Z and Curtin W A 2017 *Acta Mater.* **123** 223–34
[50] Buey D, Hector L G and Ghazisaeidi M 2018 *Acta Mater.* **147** 1–9
[51] Leyson G P M, Hector L G and Curtin W A 2012 *Acta Mater.* **60** 3873–84
[52] Morris J R, Ye Y and Yoo M H 2005 *Phil. Mag.* **85** 233–8
[53] Bettles C and Barnett M R 2012 *Advances in Wrought Magnesium Alloys: Fundamentals of Processing, Properties and Applications* (Cambridge: Woodhead Publishing) pp 105–43
[54] Ghazisaeidi M, Hector L G and Curtin W A 2014 *Acta Mater.* **80** 278–87
[55] Luque A, Ghazisaeidi M and Curtin W A 2014 *Acta Mater.* **81** 442–56
[56] Wang Y, Chen L Q, Liu Z K and Mathaudhu S N 2010 *Scr. Mater.* **62** 646–9
[57] Leyson G P M, Curtin W A, Hector L G and Woodward C F 2010 *Nat. Mater.* **9** 750–5
[58] Tehranchi A, Yin B and Curtin W A 2018 *Acta Mater.* **151** 56–66
[59] Wu Z, Yin B and Curtin W A 2016 *Acta Mater.* **119** 203–17
[60] Nie J F, Zhu Y M, Liu J Z and Fang X Y 2013 *Science* **340** 957–60
[61] Baskes M 1997 *Mater. Chem. Phys.* **50** 152–8